

Article

Cu Nanoparticles/Fluorine-Doped Tin Oxide (FTO) Nanocomposites for Photocatalytic H₂ Evolution under Visible Light Irradiation

Hui Liu, An Wang, Quan Sun, Tingting Wang * and Heping Zeng *

Key Laboratory of Functional Molecular Engineering of Guangdong Province, School of Chemistry & Chemical Engineering, South China University of Technology, Guangzhou 510640, China; cehuilu@mail.scut.edu.cn (H.L.); ceakwong@mail.scut.edu.cn (A.W.); boldymansun@163.com (Q.S.)

* Correspondence: ttwang@scut.edu.cn (T.W.); hpzeng@scut.edu.cn (H.Z.);
Tel.: +86-208-711-2631 (T.W.); +86-208-711-2631 (H.Z.)

Received: 12 August 2017; Accepted: 29 September 2017; Published: 12 December 2017

Abstract: Copper nanoparticles/fluorine-doped tin oxide (FTO) nanocomposites were successfully prepared by a simple hydrothermal method. The synthesized nanocomposites were characterized by X-ray diffraction (XRD), UV-visible diffuse-reflectance spectrum (UV-VIS DRS), energy dispersive X-ray (EDX), transmission electron microscopy (TEM), Raman spectra, and X-ray photoelectron spectroscopy (XPS). The obtained Cu/FTO nanocomposites exhibit high photocatalytic activity for H₂ evolution under visible light ($\lambda > 420$ nm) irradiation. When the content of Cu is 19.2 wt % for FTO, the Cu/FTO photocatalyst shows the highest photocatalytic activity and the photocatalytic H₂ evolution rate is up to 11.22 $\mu\text{mol}\cdot\text{h}^{-1}$. Meanwhile, the photocatalyst exhibits excellent stability and repeatability. It is revealed that the transfer efficiency of the photogenerated electrons is improved greatly because of the intense interaction between Cu NPs and FTO. Furthermore, a possible mechanism is proposed for enhanced photocatalytic H₂ evolution of Cu/FTO photocatalysts under visible light irradiation.

Keywords: Cu nanoparticles; Cu/FTO nanocomposites; H₂ evolution; visible light; transfer efficiency

1. Introduction

Hydrogen (H₂) is regarded as one of the most promising energy sources because of its high energy content per mass. Photocatalytic H₂ evolution using solar energy has attracted much attention, which is a feasible method to solve energy shortages and environmental crises [1–3]. Since Fujishima and Honda firstly reported the photolysis of water based on TiO₂ electrodes in 1972 [4], semiconductor materials as photocatalysts have been extensively studied for highly-efficient solar water splitting. Subsequently, many semiconductor materials have been developed as efficient photocatalysts to make the utmost of solar energy for photocatalytic H₂ evolution [5,6].

It is well known that tin oxide (SnO₂) is one of the most promising semiconductors for photocatalytic H₂ evolution due to its excellent chemical and physical properties [7]. In the past few decades, SnO₂ has been extensively used in gas sensing, photoelectric conversion and photocatalysis, etc. However, because of the intrinsic band gap (ca. 3.6 eV), SnO₂ cannot fully use solar radiation in visible spectrum [8]. Many researchers have been trying to modify SnO₂ to increase its absorption of visible light, which accounts for 45% of sunlight [9]. Many different approaches can be used to promote visible light absorption, such as metal doping, ion doping, carbon materials doping, etc. [10–12]. Especially, fluorine (F) has been considered as one of the most effective dopants for enhancing light absorption. Fluorine-doped tin oxide (FTO) is widely used as conducting electrodes for photoelectrochemical reactions [13]. However, owing to the rapid recombination that photoinduction carries, the photocatalytic activity of fluorine-doped tin oxide (FTO) for H₂ evolution is usually very low, or non-existent, in the presence of a sacrificial agent [14].

As it is well known, loading metal nanoparticles (NPs) as co-catalysts on the surface of catalysts is one of the most effective ways to increase the separation efficiency of photoinduced electron-hole pairs [15]. Many researchers reported that metals, such as Au, Ag, Pt, Cu, and Pd, could be used to promote the migration efficiency of electrons [16–20]. Among of them, Cu has attracted much more attention because of its low cost and abundance [21]. Additionally, Cu NPs can generate the localized surface plasmon resonance (LSPR) effect and it is beneficial for the separation of photoinduced electron-hole pairs, which can greatly enhance the photocatalytic activity [22]. Therefore, Cu NPs as co-catalyst-modified semiconductor photocatalysts may be a promising system to promote the migration of photoinduced electrons for enhancing photocatalytic H₂ evolution. Though there are many reports about growth of copper or copper oxides on FTO for photoelectrochemical hydrogen evolution reaction (HER) and oxygen evolution reaction (OER) [23,24]. To the best of our knowledge, there is no report about Cu NP-modified FTO (Cu/FTO) nanocomposites for photocatalytic H₂ evolution under visible light irradiation.

Here, based on our previous research [15,22,25,26], we reported that FTO nanopowders were fabricated by a typical sol-gel method and then modified with Cu further by a facile hydrothermal method. The Cu/FTO nanocomposites were characterized by X-ray diffraction (XRD), UV-VIS, energy dispersive X-ray (EDX), transmission electron microscopy (TEM), X-ray photoelectron spectroscopy (XPS) and so forth. The photocatalytic H₂ evolution of Cu/FTO nanocomposites was evaluated under visible light illumination. The F dopant can greatly enhance the absorption ability of the visible light of SnO₂ and the Cu/FTO nanocomposites exhibit high photocatalytic activity for H₂ evolution. Furthermore, the possible factors in the improvement of photocatalytic activity were also investigated and discussed in this paper.

2. Results

2.1. Crystal Structure and Composition

Figure 1 shows the XRD patterns of as-prepared samples. For pure SnO₂, the diffraction peaks are indexed to the crystalline tetragonal structure of SnO₂ (JCPDS No. 41-1445) [27]. The FTO sample exhibits similar diffraction peaks with pure SnO₂, which indicates FTO has the similar crystal structure with pure SnO₂. For Cu/FTO samples, the diffraction peaks at 43.3°, 50.5°, and 74.1° are assigned to the (111), (200), and (220) planes of face-centered cubic Cu (JCPDS No. 04-0836) [26]. As the content of Cu increases, the intensity of characteristic peaks becomes stronger. No diffraction peak of CuO or Cu₂O is observed, which is in agreement with the result of the XPS analysis below. Additionally, the XRD patterns of FTO after the introduction of Cu show no significant change indicating that the introduction of Cu does not influence the crystal structure of FTO.

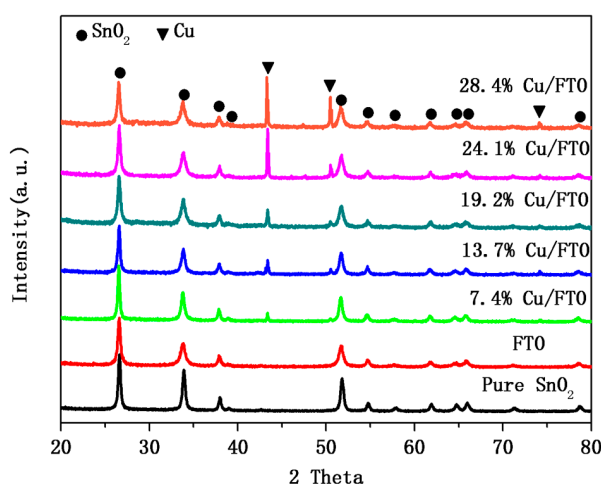


Figure 1. XRD (X-ray diffraction) patterns of pure SnO₂, FTO (Fluorine-doped tin oxide), and Cu/FTO samples with different contents of Cu.

To elaborate on the information of the as-prepared samples, Fourier transform infrared spectroscopy (FTIR) was carried out. Figure 2 depicts the FTIR spectra of pure SnO₂, FTO, and 19.2% Cu/FTO. The peaks at 924 cm⁻¹ and 1530 cm⁻¹ can be ascribed to the N–H out-of-plane bending vibration and in-plane bending vibration. The peak at 1678 cm⁻¹ is attributed to the C=O stretching vibration [28]. The peaks around 3400–3800 cm⁻¹ correspond to the N–H stretching vibration of amino groups and the O–H stretching vibrations of absorbed molecular water [6]. The characteristic peaks at 495 cm⁻¹ and 642 cm⁻¹ are ascribed to the O–Sn–O stretching vibration and the Sn–O stretching vibration, respectively [29]. The main characteristic peaks of SnO₂ are apparent in Cu/FTO nanocomposites, indicating the structure of SnO₂ remains relatively intact. Moreover, no peak of Cu is observed because Cu is not active for infrared spectra.

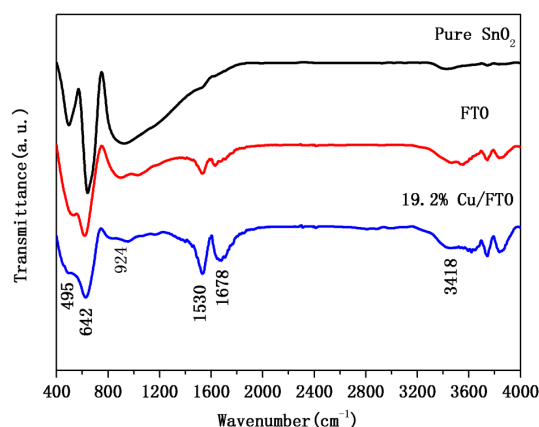


Figure 2. FTIR (Fourier transform infrared spectroscopy) spectra of pure SnO₂, FTO, and Cu/FTO samples.

Figure 3 displays the Raman spectra of pure SnO₂, FTO, and Cu/FTO. There are three fundamental Raman scattering peaks in good agreement with those of rutile SnO₂ single crystal [7]. For pure SnO₂, the characteristic and strong band at 625 cm⁻¹ is attributed to A_{1g} vibration mode of SnO₂. The weak bands around 478 cm⁻¹ and 772 cm⁻¹ correspond to E_g and B_{2g} vibration modes of SnO₂ [30]. After doping F ions, the dominant bands of SnO₂ broaden and have a slight shift, which might be evidence that F ions have substituted for a portion of O²⁻ in the SnO₂. Compared with FTO, the intensity of Cu/FTO samples become stronger, indicating that there may be an intense interaction between Cu NPs and FTO [22]. Especially, the 19.2% Cu/FTO sample exhibits the strongest intensity and this SERS enhancement may be due to surface plasmon resonance [31]. Moreover, Figure S1 shows the Raman spectra at low wavelength region. Compared with FTO, there is no other band appearing for 19.2% Cu/FTO, which may exclude the presence of oxidized Cu [32].

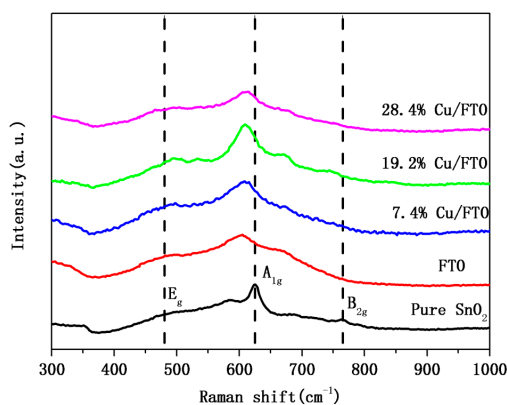


Figure 3. Raman spectra of pure SnO₂, FTO and Cu/FTO samples.

Morphologies and microstructures of the samples were studied by scanning electron microscopy (SEM), transmission electron microscopy (TEM), and high resolution TEM (HRTEM). Figure 4a shows the SEM image of the FTO sample. The morphology looks like irregular particles and many aggregations exist. Figure 4b–e shows the SEM images of Cu/FTO (7.4%, 19.2%, and 28.4%) samples, respectively. After the introduction of Cu, the particle size of Cu/FTO samples seems to be larger and there appear to be more aggregations. Especially for the 28.4% Cu/FTO sample, bulk agglomeration appears in the image (Figure 4e). The EDX spectrum (Figure 4f) and the elemental mapping patterns (Figure 4g) confirm that C, O, Sn, Cu, and F exist, which is consistent with the result of XPS below. Meanwhile, we can see that the main elements are uniformly distributed. The TEM images (Figure S2a–c) shows that the size distribution of 19.2% Cu/FTO sample is about 40–80 nm and there are some particles joining together. The HRTEM image of 19.2% Cu/FTO is presented in Figure S2d. The lattice spacing of $d = 0.209$ nm corresponds to the (111) plane of Cu [15]. The lattice spacing of $d = 0.237$ nm and 0.335 nm are attributed to the (200) plane and the (110) plane of SnO₂ (JCPDS No. 41-1445), respectively [33]. It can be found that Cu NPs and FTO have a close contact for developing the heterogeneous interface and this can promote the migration efficiency of photoinduced electrons.

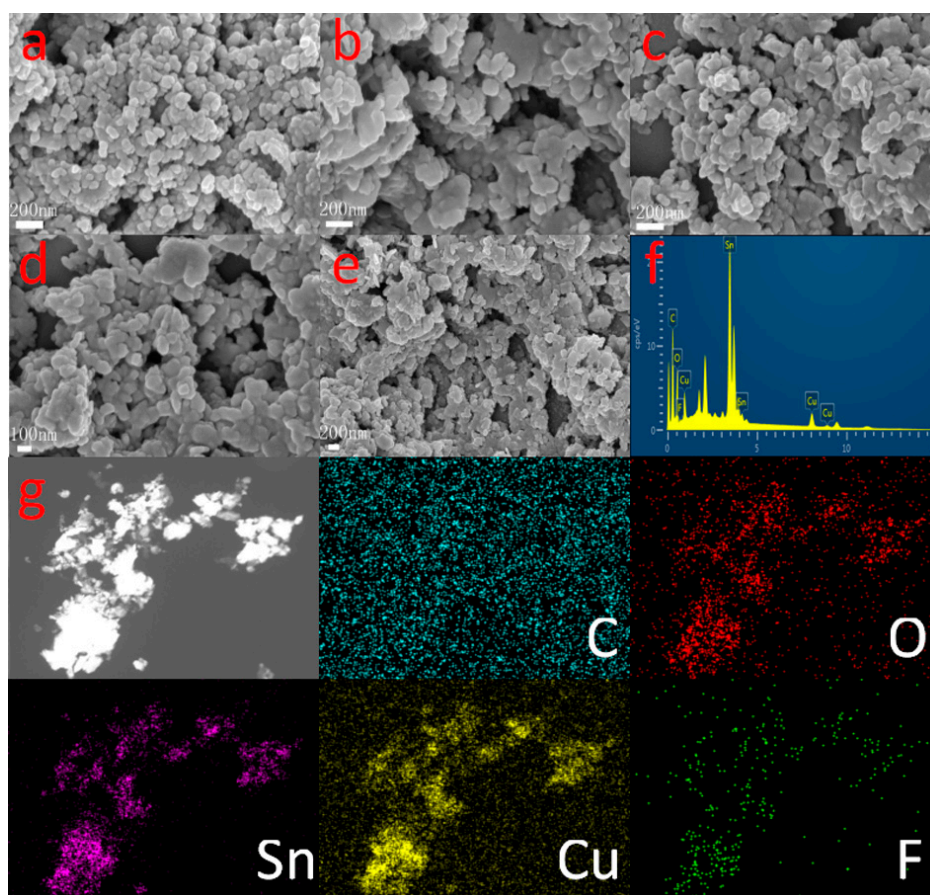


Figure 4. SEM (scanning electron microscopy) images (a) FTO; (b) 7.4% Cu/FTO; (c,d) 19.2% Cu/FTO; (e) 28.4% Cu/FTO; EDX (energy dispersive X-ray) spectrum (f); and elemental mapping patterns (g) of the 19.2% Cu/FTO sample.

The XPS spectra of the as-prepared 19.2% Cu/FTO sample were analyzed to further determine the chemical composition and the chemical state of elements. The results are shown in Figure 5. The standard C 1s peak at 284.8 eV was used as a reference to correct the peak shifts. The survey spectra of Cu/FTO sample (Figure 5a) suggest the presence of C, O, F, Sn, and Cu elements. Figure 5b shows the high-resolution XPS spectra of C 1s, the peaks at 284.8 eV, 285.9 eV, and 288.6 eV correspond

to C–C, C–O, and O–C=O, respectively [34]. The XPS spectrum of O 1s (Figure 5c) exhibits two fitted peaks located at 531.1 eV and 532.2 eV, which are assigned to Sn–O and C–O. The XPS spectrum of Sn 3d (Figure 5d) shows two peaks attributed to Sn 3d_{5/2} and Sn 3d_{3/2}. The first signal peak can be fitted into two peaks at 486.9 eV and 487.4 eV, which can be ascribed to Sn–O and Sn–F, respectively. The F 1s spectrum (Figure S3) exhibits only one major peak, which is assigned to F–Sn bond [14,35]. As shown in Figure 5f, the characteristic peaks of Cu 2p at 932.5 eV and 952.6 eV correspond to the binding energy of Cu 2p_{3/2} and Cu 2p_{1/2}, respectively. The characteristic satellite peaks are not observed, suggesting that the high value state of Cu²⁺ is inexistence. Giving that the XPS spectra of Cu 2p is not able to distinguishing Cu⁺ or Cu⁰, Cu 2p Auger electron spectroscopy (AES) was carried out by XPS. As illustrated in Figure 5f, the only peak at 918.6 eV is assigned to Cu⁰ rather than Cu⁺, which is accordance with the result of the XRD analysis [15,25,27]. The abovementioned results show that the Cu²⁺ species are fully reduced to Cu⁰ rather than Cu⁺, which is consistent with the results of the XRD and Raman analysis.

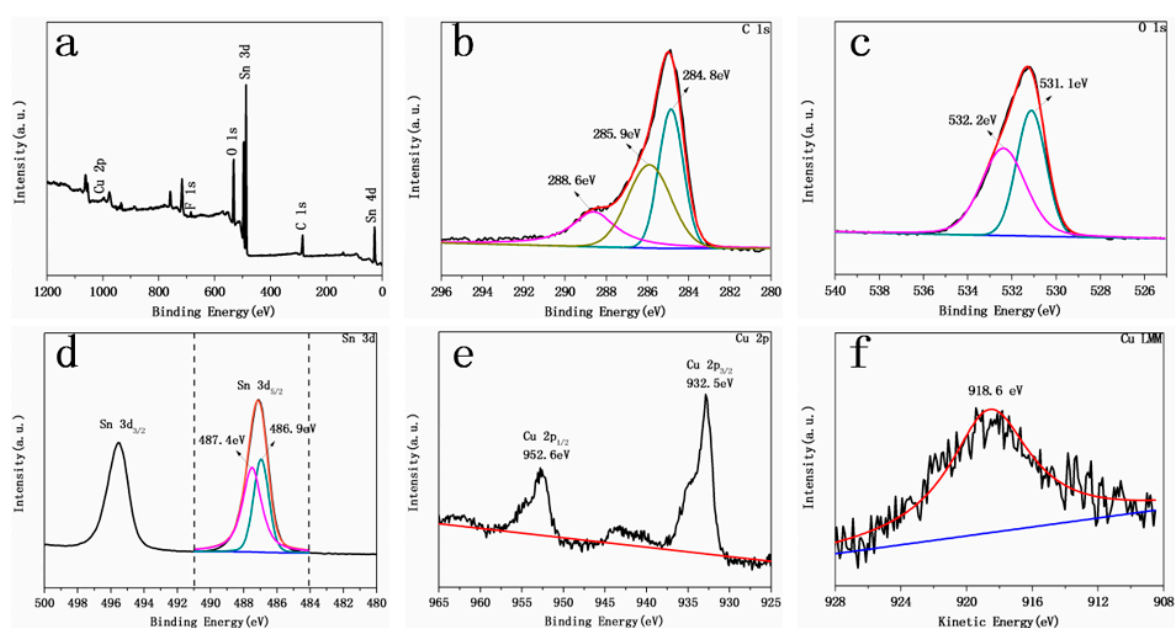


Figure 5. XPS (X-ray photoelectron spectroscopy) spectra of 19.2% Cu/FTO sample. (a) Survey spectra; (b) C 1s; (c) O 1s; (d) Sn 3d; (e) Cu 2p; and (f) Cu 2p AES (Auger electron spectroscopy).

2.2. Optical and Photoelectrochemical Properties

To investigate the optical property of pure SnO₂, FTO, and Cu/FTO samples, UV-VIS diffuse reflectance spectra was carried out. As displayed in Figure S4a, pure SnO₂ has a limited visible light absorption for itself because of its intrinsic band gap. However, after doping F ions, FTO exhibits strong absorption in the visible light range, which is beneficial for enhancing the H₂ evolution under visible light irradiation.

The optical band gap of semiconductors was determined by the Tauc equation [36]:

$$(\alpha h\nu)^n = A(h\nu - E_g)$$

where α is the absorption coefficient, $h\nu$ is the photon energy, A and n are constant, E_g is the optical band energy. The value of n is 0.5 and 2 for the indirect and direct band gap, respectively [37]. The E_g was calculated by the intercept of the extrapolated linear part of the curve with the energy axis. As presented in Figure S4b, the value of n is 2 and the band gap values of pure SnO₂ and FTO are 3.51 eV and 2.26 eV, respectively. As depicted in Figure 6, after the introduction of Cu, the absorption

intensity of Cu/FTO samples is improved greatly in the visible light region. Furthermore, the 19.2% Cu/FTO sample exhibits the best absorption in the visible light region.

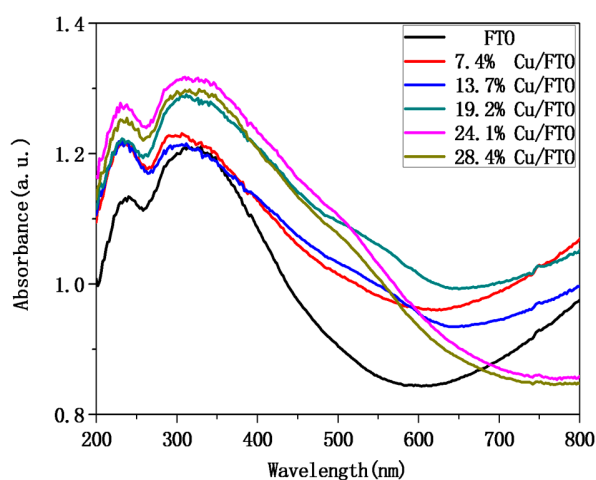


Figure 6. UV-VIS DRS (UV-visible diffuse-reflectance spectrum) of FTO and Cu/FTO samples.

To study the interaction between Cu NPs and FTO, we performed photoluminescence (PL) spectra and the results are presented in Figure 7. As displayed, all the samples of FTO and Cu/FTO exhibit a similar emission spectra shape with different intensities. The FTO shows the highest emission peak attributed to its higher recombination of the photogenerated electron-hole pairs. The emission intensity decreases with the introduction of Cu, indicating that the recombination of photogenerated electron-hole pairs is restrained in the Cu/FTO. This phenomenon could be due to the fast transfer of electrons from the FTO to the Cu and this could enhance the photocatalytic activity. Especially, the 19.2% Cu/FTO sample has the lowest emission intensity, suggesting that it may have the optimal content of Cu to inhibit carrier recombination, and this is consistent with the result of the photocatalytic H₂ evolution experiment. Due to the lower charge's recombination, more electrons will participate in photocatalytic reaction and, thus, enhance photocatalytic H₂ evolution. However, when further increasing the content of Cu, the Cu/FTO samples exhibit an increase tendency in emission intensity. The reason may be that the introduction of excessive Cu results in serious agglomeration, which could inhibit the fast migration of electrons [11].

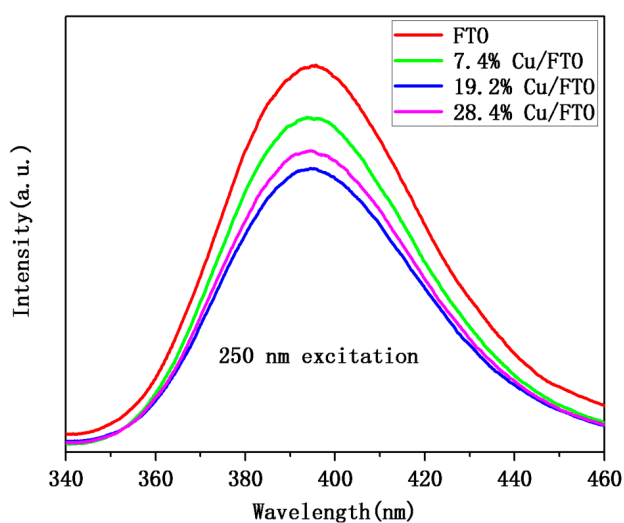


Figure 7. PL (photoluminescence) spectra of FTO and Cu/FTO samples with different contents of Cu.

As we know, the photocurrent test of semiconductors can be used to evaluate the separation and transfer efficiency of photogenerated electron–hole pairs. Figure 8a shows the transient photocurrent response of FTO and Cu/FTO film electrodes for six on-off cycles under visible light irradiation. Upon light irradiation, the photocurrent response appears in all FTO and Cu/FTO samples, but when the light is turned off, the value of the photocurrent decreases quickly to zero, which is reproducible in the six on-off cycles. The Cu/FTO samples show higher photocurrent density than that of FTO, indicating that there is less carrier recombination and much faster transfer of charges due to the intense surface interaction between Cu and FTO. Moreover, the 19.2% Cu/FTO sample exhibits the highest photocurrent density and the value is about 4.5 times as high as that of bare FTO. All these results evidently indicate the separation efficiency and transfer of the photogenerated electron–hole pairs are enhanced significantly by the introduction of Cu.

In order to further investigate the charge transfer capability, the EIS (electrochemical impedance spectra) Nyquist plots of both FTO and Cu/FTO samples were obtained and presented in Figure 8b. Generally, the smaller the diameter is, the lower charge transfer resistance and the faster interface charge transfer are. Compared with FTO, the Cu/FTO samples show smaller diameter, indicating that the introduction of Cu can diminish the impedance. Furthermore, the 19.2% Cu/FTO sample shows the smallest diameter due to its lower impedance. This result is consistent with that received by the photocurrent analysis.

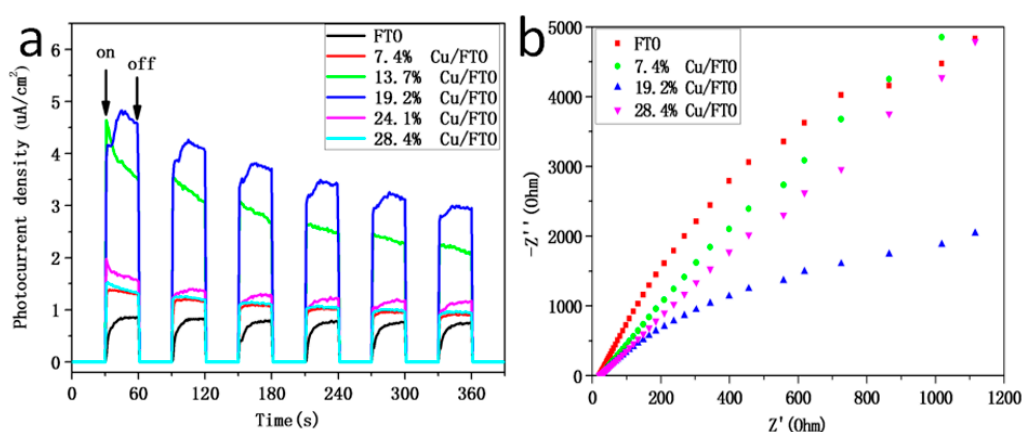


Figure 8. (a) The transient photocurrent of FTO and Cu/FTO samples with different contents of Cu and (b) EIS (electrochemical impedance spectra) Nyquist plots of FTO and Cu/FTO samples with different contents of Cu under visible light irradiation.

2.3. Photocatalytic Hydrogen Evolution

The photocatalytic hydrogen evolution of samples is evaluated under visible light irradiation with lactic acid as the sacrificial agent. There is no H_2 evolution of all samples to be detected without light irradiation, suggesting that H_2 evolution arises from photocatalytic reactions.

On one hand, when the content of Cu is 19.2%, we performed a series of photocatalytic H_2 evolution experiments under visible light irradiation to determine the optimal content of F. Figure 9 shows photocatalytic H_2 evolution rates of 19.2% Cu/ SnO_2 and 19.2% Cu/FTO with different Sn/F molar ratios under visible light irradiation. Compared with 19.2% Cu/ SnO_2 , all the 19.2% Cu/FTO samples with different Sn/F molar ratios exhibit higher photocatalytic activity of H_2 evolution. Moreover, when the Sn/F molar ratios is 10:5, the 19.2% Cu/FTO sample achieves the highest photocatalytic H_2 evolution rate ($11.22 \mu\text{mol h}^{-1}$), which could be ascribed to the appropriate band gap and fewer defect sites of FTO (Sn/F = 10:5) than other FTO samples [37].

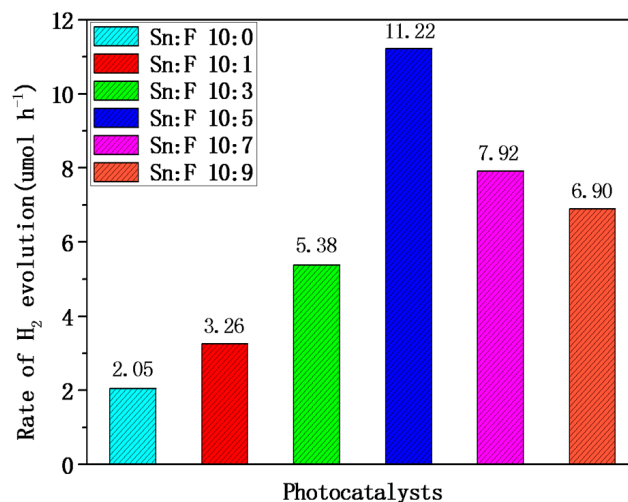


Figure 9. Photocatalytic H₂ evolution rates of 19.2% Cu/SnO₂ and 19.2% Cu/FTO samples with different Sn/F molar ratios under visible light irradiation.

On the other hand, when the Sn/F molar ratio is 10:5, we performed a series of photocatalytic H₂ evolution experiments under visible light irradiation to determine the optimal content of Cu in the Cu/FTO samples and the results were shown in Figure 10. The bare FTO sample does not show any photocatalytic activity of H₂ evolution, which may be due to the fast recombination of photoinduced electron-hole pairs. However, after the introduction of Cu, the Cu/FTO samples exhibit excellent photocatalytic activity of H₂ evolution. The H₂ evolution rate of Cu/FTO samples increases with the content of Cu and the highest photocatalytic H₂ evolution rate is up to 11.22 μmol·h⁻¹ when the content of Cu is 19.2 wt % for FTO. However, when the content of Cu reach 19.2%, the H₂ evolution rate of Cu/FTO decreases with further increasing content of Cu. The results suggest the appropriate content of Cu can enhance photocatalytic activity because of the high absorption of light and the faster transfer of electrons. However, the introduction of excessive Cu may aggregate together and become new recombination centers of photogenerated electron-hole pairs, which could inhibit the photocatalytic activity of H₂ evolution [38]. This result is consistent with the result of the PL spectra (Figure 7).

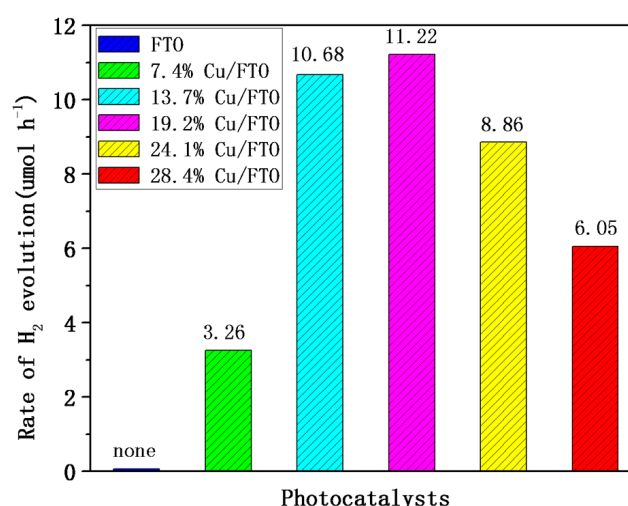


Figure 10. Photocatalytic H₂ evolution rate of FTO (Sn/F = 10/5) and Cu/FTO (Sn/F = 10/5) with different contents of Cu.

Considering practical applications, the representative 19.2% Cu/FTO sample was selected to investigate the recycling and stability of Cu/FTO samples. As shown in Figure 11, the recycling photocatalytic test was carried out for six runs under the same condition. The photocatalytic H₂ evolution of the sample is steady for six repeated runs under visible light irradiation, suggesting that the as-prepared Cu/FTO samples have excellent stability and repeatability. Furthermore, no obvious change of XRD patterns (Figure S5) before and after the stability test is observed, indicating the photocatalysts have good stability during photocatalytic H₂ evolution [34].

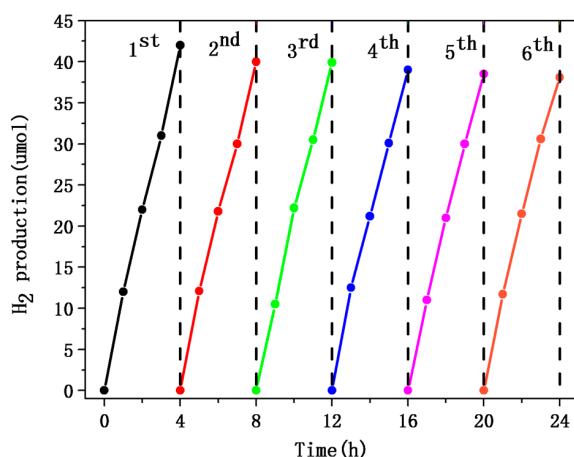


Figure 11. Recycling test of as-prepared 19.2% Cu/FTO (Sn/F = 10/5) under visible light irradiation for H₂ evolution (irradiation time = 24 h).

2.4. Mechanism

On the basis of all the above results and discussions, the proposed schematic mechanism of photocatalytic H₂ evolution of Cu/FTO photocatalyst is illustrated in Figure 12. Upon visible light irradiation, the electrons (e^-) of the valence band (VB) can be excited to the conduction band (CB) and the holes (h^+) remain in the valence band (VB). Due to the fast recombination of photogenerated electron-hole pairs, the photocatalytic activity of naked FTO is very low. However, after the introduction of Cu NPs, the recombination of photogenerated electron-hole pairs is greatly inhibited. Due to the existence of trapping centers (Cu NPs), the electrons (e^-) from the conduction band (CB) are tend to transfer quickly to Cu NPs and then react with H^+ for H₂ more easily. Meanwhile, the holes (h^+) are consumed by the sacrificial reagents (lactic acid). Thereby, the as-prepared Cu/FTO photocatalyst is beneficial for photocatalytic H₂ evolution.

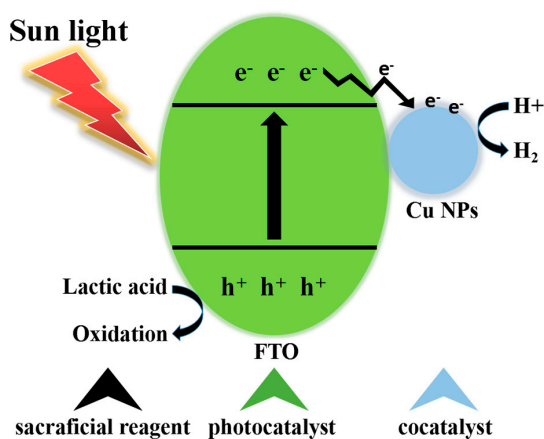


Figure 12. Schematic mechanism for photocatalytic H₂ evolution on the Cu/FTO system.

3. Materials and Methods

3.1. Materials

All the chemical reagents and solvents were analytical grade and used without further purification. Deionized water was supplied by a Millipore Milli-Q system (Millipore, Suzhou, China). Copper acetate hydrate ($\text{Cu}(\text{CH}_3\text{COO})_2 \cdot \text{H}_2\text{O}$, $\geq 99.0\%$), tin chloride dehydrate ($\text{SnCl}_2 \cdot 2\text{H}_2\text{O}$, $\geq 98.0\%$), hydrofluoric acid (HF , $\geq 40\%$), ammonium hydroxide ($\text{NH}_3 \cdot \text{H}_2\text{O}$, $\geq 25\%$), lactic acid ($\text{C}_3\text{H}_6\text{O}_3$, $\geq 97.0\%$) and glucose ($\text{C}_6\text{H}_{12}\text{O}_6$, $\geq 98.0\%$) were purchased from Sinopharm Chemical Reagent Co. Ltd. (Dalian, China).

3.2. Synthesis of FTO Nanopowders

A typical synthesis process is as following. Firstly, 15 g of tin chloride dehydrate ($\text{SnCl}_2 \cdot 2\text{H}_2\text{O}$) was dissolved in 10 mL of deionized water and then ammonium hydroxide ($\text{NH}_3 \cdot \text{H}_2\text{O}$) was added dropwise into the solution under vigorous stirring until the pH value of the solution was up to 7. The solution was centrifuged at 9000 rpm to obtain the precipitation and the precipitation was washed three times with deionized water. Secondly, a certain amount of hydrofluoric acid (HF) was slowly dropped into the precipitation under vigorous stirring and obtained the sol mixture. Then the sol mixture was dried in a drying oven at 200 °C for 4 h and the gel mixture obtained. Finally, the gel mixture was calcined at 450 °C for 2 h under air in a muffle furnace and subsequently ground into fine nanopowders. Similarly, The FTO nanopowders with different Sn/F molar ratios (10:0, 10:1, 10:3, 10:5, 10:7, 10:9) were synthesized by following the same method. The Sn/F molar ratios (10:0, 10:1, 10:3, 10:5, 10:7, 10:9) are theoretical values calculated by the precursor ratios. If there is no special instructions in the paper, the Sn/F molar ratio of FTO is 10:5.

3.3. Synthesis of Cu/FTO Nanocomposites

In a typical synthesis process, 10 mL of deionized water, 15 mL of copper acetate (0.2 M $\text{Cu}(\text{CH}_3\text{COO})_2$), 1.2 g of glucose ($\text{C}_6\text{H}_{12}\text{O}_6$) and 800 mg of FTO nanopowders were mixed together to form a homogeneous suspension by sonicating for 30 min. Then the suspension was transferred to a Teflon-lined autoclave (SX2-12-10Q, Suzhou Jiangdong Precision Instrument Co. Ltd., Shanghai, China) and heated at 120 °C for 12 h. Finally, the resulting solution was centrifuged to obtain the solid product. The solid product was washed three times by deionized water and ethanol, respectively. The obtained product was dried in a vacuum drying oven at 50 °C for 5 h. The Cu/FTO nanocomposites with different contents of Cu (0%, 7.4%, 13.7%, 19.2%, 24.1%, 28.4%) were prepared by following the same method. Cu wt % (0%, 7.4%, 13.7%, 19.2%, 24.1%, 28.4%) is the theoretical value calculated by the precursor ratios.

3.4. Characterization

The crystalline structure of the samples was characterized by using D8 Advantage X-ray diffraction (XRD, Bruker, Beijing, China) with Cu $K\alpha$ radiation. Fourier transform infrared spectroscopy (FTIR) was recorded in the wave number range from 400 cm^{-1} to 4000 cm^{-1} by a FTIR spectrometer (Nicolet 670, Bruker, Beijing, China). The morphology of the samples was characterized by scanning electron microscopy (Merlin, Zeiss, Beijing, China). Transmission electron microscopy (TEM) test was conducted by an electron microscope (JEOL, JEM-2100, Bruker, Beijing, China) equipped with energy dispersive X-ray (EDX) spectrometer. X-ray photoelectron spectroscopy (XPS) was recorded on a Kratos Axis-Ultra DLD (Axis Ultra DLD, Bruker, Beijing, China). UV-VIS diffuse reflectance absorption spectra were obtained by a Hitachi U-3010 spectrophotometer (Shimadzu, Beijing, China). The photoluminescence spectra (PL) was conducted on a Hitachi F-4500 fluorescence spectrophotometer (Shimadzu, Beijing, China). Raman spectra were obtained by Laser Confocal Raman Microscopy system (LabRAM Aramis, H.J.Y, Beijing, China). The photocurrents and electrochemical impedance spectra (EIS) were recorded on an electrochemical workstation (CHI660C, CH Instruments, Inc., Beijing, China).

3.5. Photocatalytic Hydrogen Evolution Experiment

The photocatalytic experiment was performed by using a Xe lamp with an ultraviolet cut-off filter (PLS-SXE300CUV, Perfect light Co. Ltd., Beijing, China) ($\lambda > 420$ nm) as a light source in a quartz reaction cell, which was connected to a closed gas circulation. Based on our previous research, the as-synthesized photocatalyst (50 mg), lactic acid (10 mL), and water (60 mL) were mixed together by constant magnetic stirring (85-2, Gongyi yuhua Instrument Co. Ltd., Zhengzhou, China) to form a homogeneous suspension. The solution was evacuated with N_2 before every photocatalytic reaction. The evolved H_2 under irradiation was analyzed by online gas chromatography (GC-7900, Tianmei Co. Ltd., Beijing, China) with a thermal conductivity detector (TCD).

3.6. Photoelectrochemical Measurements

Electrochemical measurements were performed by using an electrochemical workstation (CHI660C Instruments, Shanghai, China). FTO and Cu/FTO electrodes served as the working electrode, platinum wire was used as the counter electrode, and Ag/AgCl as the reference electrode. The 0.5 M Na_2SO_4 aqueous solution served as the electrolyte and a 300 W Xe lamp was used as the light source. The working electrode was prepared as follows: 0.1 g of as-synthesized catalyst was dispersed in 1 mL of ethanol solution by sonication to get slurry. Then the slurry was spread onto the cleaned ITO glass and the as-prepared electrolyte was dried at 323 K for 4 h under vacuum.

4. Conclusions

In summary, we prepared a series of FTO nanopowders with different Sn/F molar ratios by a typical sol-gel method and then they were modified with different contents of Cu via a facile hydrothermal method. Compared with pure SnO_2 , the fluorine-doped tin oxide (FTO) exhibits stronger absorption in the visible light range, but it does not show any photocatalytic activity for H_2 evolution because of the fast recombination of photogenerated electron-hole pairs. However, after the introduction of Cu, the Cu/FTO nanocomposites show excellent photocatalytic activity for H_2 evolution. When the loading content of Cu is 19.2 wt % for FTO, the highest H_2 evolution rate is up to $11.22 \mu\text{mol h}^{-1}$ under visible light irradiation. The photocatalysts exhibit excellent stability and repeatability for H_2 evolution. Moreover, the introduction of Cu could greatly promote the separation and transfer efficiency of the photogenerated electron-hole pairs and, thus, can enhance photocatalytic H_2 evolution. This work provides an insight for developing effective photocatalysts, which could be used for the conversion of solar energy to new energy sources.

Supplementary Materials: The following are available online at www.mdpi.com/2073-4344/7/12/385/s1, Figure S1. Raman spectra of FTO and 19.2% Cu/FTO. Figure S2. TEM (a) and HRTEM (b) of as-prepared 19.2% Cu/FTO sample. Figure S3. F 1s spectra of 19.2% Cu/FTO with XPS characterization. Figure S4. UV-VIS diffuse reflectance spectra (a) and optical band gap spectra (b) of pure SnO_2 and FTO. Figure S5. XRD patterns of 19.2% Cu/FTO before and after the stability test of hydrogen evolution.

Acknowledgments: We gratefully acknowledge financial support from the National Natural Science Foundation of China (Nos. 21571064, 21371060) and the Fundamental Research Funds for the Central Universities (No. 2015ZM162).

Author Contributions: Heping Zeng and Hui Liu conceived and designed the experiments; Hui Liu performed the experiments; Hui Liu, An Wang, Quan Sun and Tingting Wang analyzed the data; Hui Liu wrote the paper.

Conflicts of Interest: The authors declare no conflict of interest.

References

1. Wang, Y.; Wang, Q.; Zhan, X.; Wang, F.; Safdar, M.; He, J. Visible light driven type II heterostructures and their enhanced photocatalysis properties: A review. *Nanoscale* **2013**, *5*, 8326–8339. [[CrossRef](#)] [[PubMed](#)]
2. Jafari, T.; Moharreri, E.; Amin, A.; Miao, R.; Song, W.Q.; Suib, S. Photocatalytic Water Splitting—The Untamed Dream: A Review of Recent Advances. *Molecules* **2016**, *21*, 900. [[CrossRef](#)] [[PubMed](#)]

3. Huo, J.P.; Zeng, H.P. A novel triphenylamine functionalized bithiazole–metal complex with C₆₀ for photocatalytic hydrogen production under visible light irradiation. *J. Mater. Chem. A* **2015**, *3*, 6258–6264. [[CrossRef](#)]
4. Fujishima, A.; Honda, K. Photolysis-decomposition of water at the surface of an irradiated semiconductor. *Nature* **1972**, *238*, 37–38. [[CrossRef](#)] [[PubMed](#)]
5. Huo, J.P.; Fang, L.T.; Lei, Y.L.; Zeng, G.C.; Zeng, H.P. Facile preparation of yttrium and aluminum co-doped ZnO via a sol–gel route for photocatalytic hydrogen production. *J. Mater. Chem. A* **2014**, *2*, 11040–11044. [[CrossRef](#)]
6. Qin, J.Y.; Huo, J.P.; Zhang, P.Y.; Zeng, J.; Wang, T.T.; Zeng, H.P. Improving the photocatalytic hydrogen production of Ag/g-C₃N₄ nanocomposites by dye-sensitization under visible light irradiation. *Nanoscale* **2016**, *8*, 2249–2259. [[CrossRef](#)] [[PubMed](#)]
7. Chen, Z.W.; Pan, D.Y.; Li, Z.; Jiao, Z.; Wu, M.H.; Shek, C.; Wu, C.M.L.; Lai, J.K.L. Recent Advances in Tin Dioxide Materials: Some Developments in Thin Films, Nanowires, and Nanorods. *Chem. Rev.* **2014**, *114*, 7442–7486. [[CrossRef](#)] [[PubMed](#)]
8. Khan, M.M.; Ansari, S.A.; Khan, M.E.; Ansari, M.O.; Min, B.K. Visible light-induced enhanced photoelectrochemical and photocatalytic studies of gold decorated SnO₂ nanostructures. *New J. Chem.* **2015**, *39*, 2758–2766. [[CrossRef](#)]
9. Babu, B.; Kadam, A.N.; Ravikumar, R.; Chan, B. Enhanced visible light photocatalytic activity of Cu-doped SnO₂ quantum dots by solution combustion synthesis. *J. Alloys Compd.* **2017**, *703*, 330–336. [[CrossRef](#)]
10. Ghimbeu, C.M.; Lumbreras, M.; Siadat, M.; van Landschoot, R.C.; Schoonman, J. Electrostatic sprayed SnO₂ and Cu-doped SnO₂ films for H₂S detection. *Sens. Actuators B Chem.* **2008**, *133*, 694–698. [[CrossRef](#)]
11. Chandra, S.; George, G.; Ravichandran, K.; Thirumurugan, K. Influence of simultaneous cationic (Mn) and anionic (F) doping on the magnetic and certain other properties of SnO₂ thin films. *Surf. Interface* **2017**, *7*, 39–46. [[CrossRef](#)]
12. Seema, H.; Christian, K.K.; Chandra, V.; Kim, K.S. Graphene-SnO₂ composites for highly efficient photocatalytic degradation of methylene blue under sunlight. *Nanotechnology* **2012**, *23*, 355705. [[CrossRef](#)] [[PubMed](#)]
13. Kent, C.A.; Concepcion, J.J.; Dares, C.J.; Torelli, D.A.; Rieth, A.J.; Miller, A.S.; Meyer, T.J. Water Oxidation and Oxygen Monitoring by Cobalt-Modified Fluorine-Doped Tin Oxide Electrodes. *J. Am. Chem. Soc.* **2013**, *135*, 8432–8435. [[CrossRef](#)] [[PubMed](#)]
14. Samad, W.Z.; Goto, M.; Kanda, H.; Nordin, N.; Liew, K.H.; Yarmo, M.A.; Yusop, M.R. Fluorine-doped tin oxide catalyst for glycerol conversion to methanol in sub-critical water. *J. Supercrit. Fluids* **2017**, *120*, 366–378. [[CrossRef](#)]
15. Zhang, P.Y.; Song, T.; Wang, T.T.; Zeng, H.P. In-situ synthesis of Cu nanoparticles hybridized with carbon quantum dots as a broad spectrum photocatalyst for improvement of photocatalytic H₂ evolution. *Appl. Catal. B Environ.* **2017**, *206*, 328–335. [[CrossRef](#)]
16. He, W.; Kim, H.K.; Wamer, W.G.; Melka, D.; Callahan, J.H. Photogenerated Charge Carriers and Reactive Oxygen Species in ZnO/Au Hybrid Nanostructures with Enhanced Photocatalytic and Antibacterial Activity. *J. Am. Chem. Soc.* **2014**, *136*, 750–757. [[CrossRef](#)] [[PubMed](#)]
17. Logar, M.; Jancar, B.; Sturm, S.; Suvorov, D. Weak polyion multilayer-assisted in situ synthesis as a route toward a plasmonic Ag/TiO₂ photocatalyst. *Langmuir* **2010**, *26*, 12215–12224. [[CrossRef](#)] [[PubMed](#)]
18. Shiraishi, Y.; Kofuji, Y.; Kanazawa, S.; Sakamoto, H.; Ichikawa, S.; Tanaka, S.; Hirai, T. Platinum nanoparticles strongly associated with graphitic carbon nitride as efficient co-catalysts for photocatalytic hydrogen evolution under visible light. *Chem. Commun.* **2014**, *50*, 15255–15258. [[CrossRef](#)] [[PubMed](#)]
19. Zou, Y.L.; Kang, S.; Li, X.Q.; Qin, L.X.; Mu, J. TiO₂ nanosheets loaded with Cu: A low-cost efficient photocatalytic system for hydrogen evolution from water. *Int. J. Hydrog. Energy* **2014**, *39*, 15403–15410. [[CrossRef](#)]
20. Han, C.; Yang, M.Q.; Zhang, N.; Xu, Y.J. Enhancing the visible light photocatalytic performance of ternary CdS–(graphene–Pd) nanocomposites via a facile interfacial mediator and co-catalyst strategy. *J. Mater. Chem. A* **2014**, *2*, 19156–19166. [[CrossRef](#)]
21. Liu, E.Z.; Qi, L.L.; Bian, J.J.; Chen, Y.H.; Hu, X.Y.; Fan, J.; Liu, H.C.; Zhu, C.J.; Wang, Q.P. A facile strategy to fabricate plasmonic Cu modified TiO₂ nano-flower films for photocatalytic reduction of CO₂ to methanol. *Mater. Res. Bull.* **2015**, *68*, 203–209. [[CrossRef](#)]

22. Huo, J.P.; Zeng, H.P. Copper nanoparticles embedded in the triphenylamine functionalized bithiazole–metal complex as active photocatalysts for visible light-driven hydrogen evolution. *J. Mater. Chem. A* **2015**, *3*, 17201–17208. [[CrossRef](#)]
23. Yang, Y.; Xu, D.; Wu, Q.Y.; Diao, P. Cu₂O/CuO Bilayered Composite as a High-Efficiency Photocathode for Photoelectrochemical Hydrogen Evolution Reaction. *Sci. Rep.* **2016**, *6*, 35158. [[CrossRef](#)] [[PubMed](#)]
24. Liu, X.; Cui, S.S.; Sun, Z.J.; Du, P.W. Copper oxide nanomaterials synthesized from simple copper salts as active catalysts for electrocatalytic water oxidation. *Electrochim. Acta* **2015**, *160*, 202–208. [[CrossRef](#)]
25. Zhang, P.Y.; Wang, T.T.; Zeng, H.P. Design of Cu-Cu₂O/g-C₃N₄ nanocomponent photocatalysts for hydrogen evolution under visible light irradiation using water-soluble Erythrosin B dye sensitization. *Appl. Surf. Sci.* **2017**, *391*, 404–414. [[CrossRef](#)]
26. Liu, H.Y.; Wang, T.T.; Zeng, H.P. CuNPs for Efficient Photocatalytic Hydrogen Evolution. *Part. Part. Syst. Character.* **2015**, *32*, 869–873. [[CrossRef](#)]
27. Zheng, L.R.; Zheng, Y.H.; Chen, C.Q.; Zhan, Y.Y.; Lin, X.Y.; Zheng, Q.; Wei, K.M.; Zhu, J.F. Network Structured SnO₂/ZnO Heterojunction Nanocatalyst with High Photocatalytic Activity. *Inorg. Chem.* **2009**, *48*, 1819–1825. [[CrossRef](#)] [[PubMed](#)]
28. Zhu, S.J.; Meng, Q.N.; Wang, L.; Zhang, J.H.; Song, Y.B.; Jin, H.; Zhang, K.; Sun, H.C.; Wang, H.Y.; Yang, B. Highly Photoluminescent Carbon Dots for Multicolor Patterning, Sensors, and Bioimaging. *Angew. Chem. Int. Ed.* **2013**, *52*, 3953–3957. [[CrossRef](#)] [[PubMed](#)]
29. Zhang, B.; Tian, Y.; Zhang, J.X.; Cai, W. The characterization of fluorine doped tin oxide films by Fourier Transformation Infrared spectrum. *Appl. Phys. Lett.* **2011**, *98*, 021906. [[CrossRef](#)]
30. Noor, N.; Parkin, I.P. Enhanced transparent-conducting fluorine-doped tin oxide films formed by Aerosol-Assisted Chemical Vapour Deposition. *J. Mater. Chem. C* **2013**, *1*, 984–996. [[CrossRef](#)]
31. Liu, E.; Kang, L.; Yang, Y.; Sun, T.; Hu, X. Plasmonic Ag deposited TiO₂ nano-sheet film for enhanced photocatalytic hydrogen production by water splitting. *Nanotechnology* **2014**, *25*, 165401–165410. [[CrossRef](#)] [[PubMed](#)]
32. Deng, Y.L.; Handoko, A.D.; Do, Y.H.; Xi, S.B.; Yeo, B.S. In Situ Raman Spectroscopy of Copper and Copper Oxide Surfaces during Electrochemical Oxygen Evolution Reaction: Identification of Cu^{III} Oxides as Catalytically Active Species. *ACS Catal.* **2016**, *6*, 2473–2481. [[CrossRef](#)]
33. Chen, X.; Zhou, B.; Yang, S.; Wu, H.; Wu, Y. In situ construction of an SnO₂/g-C₃N₄ heterojunction for enhanced visible-light photocatalytic activity. *RSC Adv.* **2015**, *5*, 68953–68963. [[CrossRef](#)]
34. Song, T.; Huo, J.P.; Liao, T.; Zeng, J.; Qin, J.Y.; Zeng, H.P. Fullerene [C₆₀] modified Cr_{2-x}Fe_xO₃ nanocomposites for enhanced photocatalytic activity under visible light irradiation. *Chem. Eng. J.* **2016**, *287*, 359–366. [[CrossRef](#)]
35. Wu, S.S.; Yuan, S.; Shi, L.Y.; Zhao, Y.; Fang, J.H. Preparation, characterization and electrical properties of fluorine-doped tin dioxide nanocrystals. *J. Colloid Interface Sci.* **2010**, *346*, 12–16. [[CrossRef](#)] [[PubMed](#)]
36. Chu, D.M.; Zhang, C.Y.; Yang, P.; Du, Y.K.; Lu, C. WS₂ as an Effective Noble-Metal Free Cocatalyst Modified TiSi₂ for Enhanced Photocatalytic Hydrogen Evolution under Visible Light Irradiation. *Catalysts* **2016**, *6*, 136. [[CrossRef](#)]
37. Yu, J.C.; Yu, J.G.; Ho, W.K.; Jiang, Z.T.; Zhang, L.Z. Effects of F⁻ Doping on the Photocatalytic Activity and Microstructures of Nanocrystalline TiO₂ Powders. *Chem. Mater.* **2002**, *14*, 3808–3816. [[CrossRef](#)]
38. Chao, Y.G.; Zheng, J.F.; Chen, J.Z.; Wang, Z.J.; Jia, S.P.; Zhang, H.X.; Zhu, Z.P. Highly efficient visible light-driven hydrogen production of precious metal-free hybrid photocatalyst: CdS@NiMoS core-shell nanorods. *Catal. Sci. Technol.* **2017**, *7*, 2798–2804. [[CrossRef](#)]

